The diurnal path to persistent convective self-aggregation

Gorm G. Jensen[1], Romain Fiévet[1], Jan O. Haerter[1,2,3]

[1]Niels Bohr Institute, Copenhagen University, Blegdamsvej 17, 2100 Copenhagen, Denmark
[2]Complexity and Climate, Leibniz Center for Tropical Marine Research, Fahrenheitstrasse 6, 28359 Bremen, Germany
[3]Jacobs University Bremen, Campus Ring 1, 28759 Bremen, Germany

Key Points:

- Diurnal surface temperature oscillations can enable convective self-aggregation in idealized simulations—especially at fine grid resolution.
- Mechanistically, strong mesoscale cold pools dry the boundary layer, which later induces irreversible dry patches in the free troposphere.
- Once formed, such dry patches can persist and intensify even if the diurnal cycle is later removed.

Corresponding author: Jan O. Haerter, `haerter@nbi.ku.dk`

Abstract

Clustering of tropical thunderstorms constitutes an important climate feedback because it influences the radiative balance. Convective self-aggregation (CSA) is a profound modeling paradigm for explaining the clustering of tropical oceanic thunderstorms. However, CSA is hampered in the realistic limit of fine model resolution when cold pools—dense air masses beneath thunderstorm clouds—are well-resolved. Studies on CSA usually assume the surface temperature to be constant, despite realistic surface temperatures varying significantly between night and day. Here we mimic the diurnal cycle in cloud-resolving numerical experiments by prescribing a surface temperature oscillation. Our simulations show that the diurnal cycle enables CSA at fine resolutions, and that the process is even accelerated by finer resolutions. We attribute these findings to vigorous combined cold pools emerging in symbiosis with mesoscale convective systems. Such cold pools suppress buoyancy in extended regions ($\sim$ 100 km) and enable the formation of persistent dry patches. Our findings help clarify how the tropical cloud field forms sustained clusters under realistic conditions and may have implications for the origin of extreme thunderstorm rainfall and tropical cyclones.

Plain Language Summary

Computer simulations of tropical clouds suggest that thunderstorms can aggregate into large-scale clusters even under homogeneous boundary conditions. This process, known as convective self-aggregation (CSA), is observed in idealized simulations. Yet, the underlying mechanisms are considered relevant for real-world atmospheric phenomena, such as tropical cyclones, and for climate feedbacks. Realism has been questioned as studies find that increasing model resolution hampers or prevents CSA. However, here we demonstrate that increasing resolution accelerates CSA if models account for surface temperature oscillations related to the natural diurnal cycle. We explain this rapid CSA with rain-induced density currents in the atmospheric boundary layer, known as cold pools. Our results may shift the CSA paradigm in favor of more realistic simulations.

1 Introduction

Convective self-aggregation (CSA) refers to the spatial separation into deep convective and dry subregions occurring spontaneously in numerical simulations with homogeneous boundary and initial conditions (Held et al., 1993; Tompkins & Craig, 1998; Bretherton et al., 2005; Wing et al., 2017). CSA serves as a plausible mechanism for observed large-scale tropical convective clustering, including the Madden-Julian oscillation (Zhang, 2005) or the formation of tropical cyclones (Emanuel, 2018; C. J. Muller & Romps, 2018). Modeling suggests that CSA typically hinges on local radiation feedbacks (C. J. Muller & Held, 2012; Emanuel et al., 2014; C. Muller & Bony, 2015; Coppin & Bony, 2015; Hohenegger & Stevens, 2016). Maintenance of CSA has been attributed to a large-scale circulation resulting in an upgradient moisture transport (Craig & Mack, 2013; Emanuel et al., 2014; C. Muller & Bony, 2015; Holloway & Woolnough, 2016). The circulation is driven by a combination of moist adiabatic lifting in the convectively active region and enhanced radiative cooling in the dry region, which must be compensated by subsidence heating.

The initial harbinger of CSA is the formation of several small persistent dry patches (Wing et al., 2017). At this initial stage, low cloud (C. J. Muller & Held, 2012) and moisture feedbacks (Emanuel et al., 2014; C. Muller & Bony, 2015) within dry regions were found to be critical for overcoming the re-distribution of moisture by negative feedbacks (Bretherton et al., 2005). Cold pools (CPs)—density currents produced by rain re-evaporation beneath thunderstorm clouds—were reported to act against such clustering (Jeevanjee & Romps, 2013; C. Muller & Bony, 2015; Boye Nissen & Haerter, 2019). Also finer hor-

izontal grid resolution, which intensifies CP effects (C. J. Muller & Held, 2012; Moseley et al., 2020; Hirt et al., 2020; Yanase et al., 2020), hampered the onset of CSA.

CSA is typically studied in the context of radiative–convective equilibrium (RCE) with constant boundary conditions in both time and space (Wing et al., 2017). The RCE framework is arguably a reasonable approximation of low-latitude oceanic conditions because sea surface temperatures exhibit only small diurnal fluctuations, especially under windy conditions (Weller & Anderson, 1996; Johnson et al., 1999). However, it is observationally evident that temporal surface temperature variations influence the spatial characteristics of convective rainfall (Chen & Houze, 1997; Dai, 2001; Kawai & Wada, 2007; Suzuki, 2009; Bellenger & Duvel, 2009; Bellenger et al., 2010; Peatman et al., 2014). For example, over tropical rain forests, where surface temperature ranges are on the order of 10 K between day and night (Sharifnezhadazizi et al., 2019), a large fraction of extreme rainfall results from mesoscale convective systems (MCSs) (Tan et al., 2015; Schumacher & Rasmussen, 2020). MCSs are defined as thunderstorm clusters exceeding 100 kilometers spatially and three hours temporally (Houze Jr, 2004). Despite indications that MCS rainfall rates and volumes might be increasing (Westra et al., 2014; Prein et al., 2017; Fowler et al., 2021), the forecast performance for MCS remains low (Fritsch & Carbone, 2004; Sukovich et al., 2014).

Several studies mimic diurnal variation through oscillating surface temperatures (Liu & Moncrieff, 1998; Tian et al., 2006; Cronin et al., 2015; Ruppert Jr & Hohenegger, 2018; Ruppert Jr & O'Neill, 2019). Under such conditions, recent simulations demonstrated the spontaneous formation of MCS-like clusters (Haerter et al., 2020), which appeared only when the surface temperature amplitude was sufficiently large ($\gtrsim 3.5\,K$). The clusters were attributed to vigorous "combined cold pools," which were able to force moist boundary layer air to the level of free convection. When the amplitude was smaller ($\lesssim 2\,K$), neither MCSs nor combined cold pools were detected, and the organizational pattern was similar to the near-random pattern during the early stages of RCE simulations. The organizational pattern observed in the presence of a large diurnal amplitude— referred to as "diurnal self-aggregation" (DSA)—is similar to CSA in that clustering occurs spontaneously and is concentrated in parts of the spatial domain. However, DSA differs from CSA as clusters organize into patterns that are anti-correlated from day to day, such that an area receiving pronounced rain on a given day will typically receive weak rain, or none at all, on the following. Haerter et al. (2020) showed that strong diurnal surface temperature oscillations concentrate convection and precipitation to occur predominantly during afternoon and evening, whereas the remainder of the day shows quiescent conditions. Despite very weak wind speed during quiescent periods the atmosphere must keep some memory in order the for convective activity to have a negative correlation from day to day. Yet, it remains to be described where and how the atmosphere stores this memory.

In search for the memory effect, this study investigates how moisture at different altitudes correlates from night to night in a numerical experiment similar to the one presented in Haerter et al. (2020). We associate the alternating dynamics of DSA with strong negative correlation of moisture around the top of the boundary layer. To our initial surprise, the analysis also reveals a strong positive moisture correlation in the free troposphere. The positive correlation is associated with the emergence of persistent dry patches closely resembling the early stage of classical CSA. A constant surface temperature control experiment shows no signs of aggregation. Our findings thus identify the diurnal cycle as a causal mechanism for this persistence.

To explore this newfound diurnal path to CSA further, we conduct a series of simulations with varying horizontal resolution. It is known that fine model resolution can hamper classical CSA (C. J. Muller & Held, 2012; Jeevanjee & Romps, 2013; C. Muller & Bony, 2015). Yet, we find that fine resolution accelerates the emergence of persistent dry patches when the surface temperature is oscillating. To explore this finding further,

we use Lagrangian particle tracking to quantify how resolution affects the CP dynamics with and without the diurnal cycle. We then draw a connection between the alternating DSA dynamics and the diurnally induced CSA by means of a case study describing the emergence of a persistent dry patch. Finally, we show that dry patches exhibit hysteresis: once formed, they persist and intensify even if the oscillations are removed. Together, our results demonstrate that surface temperature oscillations have a strong impact on persistent mesoscale organization, especially in the realistic limit of fine spatial model resolution.

2 Materials and Methods

Large-eddy model and boundary conditions. To simulate the convective atmosphere, we employ the *University of California, Los Angeles* (UCLA) Large-Eddy Simulation (LES) solver with sub-grid scale turbulence parameterized after Smagorinsky (Smagorinsky, 1963). The Coriolis force and the mean wind are both set to zero. Radiation effects are incorporated using a delta four-stream scheme (Pincus & Stevens, 2009) and a two-moment cloud microphysics scheme (Stevens et al., 2005). Rain evaporation depends on ambient relative humidity and the mean and spread of hydrometeor radii (Seifert & Beheng, 2006). Radiation interacts with the atmosphere including clouds, but does not impact the surface temperature, which is prescribed and spatially homogeneous. The prescribed surface temperature $T_s(t)$ is spatially homogeneous but oscillates temporally as

$$T_s(t) = \overline{T_s} - T_a \cos\left(2\pi\, t/t_0\right) , \tag{1}$$

where $\overline{T_s} = 298\ K$, $t_0 = 24\ h$ is the period of the simulated model day, $\overline{T_s}$ is the temporal average and T_a the amplitude of $T_s(t)$. For the simulations "DIU" $T_a = 5\ K$ is chosen, whereas for "RCE" $T_a = 0$. Insolation $S(t)$ is taken as spatially homogeneous for all simulations. For the simulations "DIU" the insolation cycle $S(t)$ oscillates temporally with an amplitude typical for the equator. For the "RCE" simulations, both $T_s(t)$ and $S(t)$ are set constant to their respective temporal averages, that is, $T_s(t) = \overline{T_s} = 298\ K$ and $S(t) = \overline{S} = 445\ W\ m^{-2}$.

Surface latent and sensible heat fluxes. Surface heat fluxes are computed interactively by standard bulk formulae and increase with the vertical temperature and humidity gradients as well as horizontal wind speed. Horizontal surface wind speed is approximated through Monin-Obukhov similarity theory (Stull, 2012). Our simulations use a simple parameterization of a homogeneous, flat land surface, by assuming surface latent heat fluxes to be reduced to 70 percent of those obtained for a saturated (sea) surface. For the DIU experiments, mean surface latent and sensible heat fluxes are $LHF \approx 57\ W/m^2$ and $SHF \approx 18\ W/m^2$, respectively, yielding a Bowen ratio of $B \approx .30$, realistic for forested land.

Initial conditions. Initial temperature and humidity are taken from observed profiles that potentially represent convective conditions (Moseley et al., 2016), but quickly self-organize during the initial spin-up. To allow the simulation to break complete spatial symmetry, the initial temperature field is perturbed by small uncorrelated noise in the lowest model layer, drawn uniformly from [-0.2,.2] K. The spin-up manifests itself in "DIU" by relatively weak precipitation during the first model day, but relatively strong precipitation during the second. From the third day on, precipitation diurnal cycles are found fairly repetitive (*compare*: Fig. 1a). Hence, over time, the system eventually establishes a self-consistent vertical temperature and moisture profile.

Model grid, dynamics, and output. The anelastic equations of motion are integrated on a regular horizontal domain with varying horizontal grid spacing dx and laterally periodic boundary conditions (Tab. 1). Vertically, the model resolution is stretched, with 100 m below 1 km, 200 m near 6 km, and 400 m in the upper layers. A sponge layer is implemented between 12.3 km and the model top, which is located at 16.5 km. Horizon-

166 tal resolution dx, domain size, and output timestep Δt_{out} vary (Tab. 1). At each out-
167 put timestep, instantaneous surface precipitation intensity, as well as instantaneous hor-
168 izontal fields of velocity and thermodynamic variables at various vertical levels are recorded.
169 Three-dimensional thermodynamic output data are recorded instantaneously at UTC
170 4, 10, 16, and 22, whereas three-dimensional velocities are recorded as time averages be-
171 tween UTC 0–6, 6–12, 12–18 and 18–24. Additionally, at 30-second and five-minute in-
172 tervals, respectively, spatially as well as horizontally averaged time series were extracted
173 from the numerical experiments.

Experiment name	Surface temperature amplitude, T_a [K]	Hor. resolution dx [km]	Domain size L [km]	Simulation period [days]	Output timestep Δt_{out} [min]
DIU-500m	5	0.5	480	0–10	15
RCE-500m	0	0.5	480	0–8	20
DIU2RCE-500m	0	0.5	480	9.75–17	15
RCE2DIU-500m	5	0.5	480	8.75–20	15
DIU-500m_small	5	0.5	240	0–18	15
RCE-500m_small	0	0.5	240	0–16	15
DIU-1km	5	1	960	0–16	20
DIU2RCE-1km	0	1	960	15.75–24	20
RCE-1km	0	1	960	0–16	20
DIU-2km	5	2	960	0–24	20
RCE-2km	0	2	960	0–20	20
DIU-4km	5	4	960	0–42	20
RCE-4km	0	4	960	0–20	20

Table 1. Summary of numerical experiments. The term "DIU" is used to indicate simulations with diurnally oscillating surface temperature $T_s(t)$ and insolation $S(t)$, whereas in "RCE" both $T_s(t)$ and $S(t)$ are held constant. The term "DIU2RCE" means that "RCE" boundary conditions are applied as a continuation of "DIU" for the respective previous period—such as DIU2RCE-500m, which is initialized with the three-dimensional atmospheric state after 9.75 days. The experiment names further include the respective horizontal model resolution.

174 **Temporal correlation.** We define the 24-hour lag correlation $C_{24h}(q_t; t, z)$ used in fig-
175 ures 1,7, S1, and S5 as the pixel-by-pixel Pearson correlation between time t and $t+24h$,
176 of the horizontal moisture distribution at the vertical level z:

$$C_{24h}(q_t; t, z) \equiv \sum_{i,j=1}^{N} \tilde{q}_t(t, x_i, y_j, z)\, \tilde{q}_t(t + 24h, x_i, y_j, z) \tag{2}$$

where $N = L/dx$ is the number of grid-boxes along the domain side length (*see* Tab. 1).
The relative spatial anomalies of q_t at time t are defined as $\tilde{q}_t(t, x, y, z) \equiv \Delta q_t(t, x, y, z)/\sigma_{q_t}(t, z)$,
where $\Delta q_t(t, x, y, z) \equiv q_t(t, x, y, z) - \langle q_t\rangle(t, z)$ is the absolute spatial anomaly of q_t and
$\langle q_t\rangle(t, z)$ its horizontal average at time t and vertical level z,

$$\langle q_t\rangle(t, z) \equiv \frac{1}{N^2} \sum_{i=1}^{N} \sum_{j=1}^{N} q_t(t, x_i, y_j, z)$$

and $\sigma_{q_t}^2$ is the horizontal variance

$$\sigma_{q_t}^2 \equiv \frac{1}{N^2} \sum_{i=1}^{N} \sum_{j=1}^{N} \left(q_t(t, x_i, y_j, z) - \langle q_t\rangle(t, z)\right)^2.$$

Note that, by definition, $C_{24h}(q_t; t, z)$ is bounded to lie between -1 and $+1$. We compare horizontal fields of $q_t(t, x, y, z)$ for various values of height z at t chosen to represent 4h of each given day. At this time of day the atmosphere is generally stably stratified, convective activity is at a minimum and the moisture field is maximally smooth. This is an advantage because we are interested in the large scale structures, and not the precise locations of individual raincells, that typically measure only few kilometers in diameter.

Coarse-graining procedure. Coarse-grained rain intensity fields, termed $\overline{R}$, are used in Fig. 3 and S4 to compute the relative standard deviation $\mathrm{RSD}(\overline{R})$, that is, the standard deviation divided by the mean, as well as the exceedance probability of daily precipitation intensity, respectively. $\overline{R}(k, l, m)$ is a three-dimensional array where each element represent a space-time cube of horizontal interval of length s and temporal interval of duration τ, that is, a cube of volume $s \times s \times \tau$. Hence,

$$\overline{R}(k, l, m) \equiv \int_{k\tau}^{(k+1)\tau} dt \int_{ls}^{(l+1)s} dx \int_{ms}^{(m+1)s} dy\ R(t, x, y),$$

where R is the model output instantaneous rainfall intensity (Tab. 1). We choose $s{=}32$ km spatially. Temporally, Fig. 3 uses $\tau{=}48$h and Fig. S4 uses $\tau{=}24$h. The interval $s{=}32$ km is a compromise between being significantly larger than typical individual deep convective rain events yet small compared to the system size. The interval $\tau{=}48$ h in Fig. 3 is chosen to emphasize persistent structures and discount the day-to-day anti-correlated, high intensity mesoscale rain clusters. The interval $\tau{=}24$ h in Fig. S4 is chosen to capture the natural timescale of one day and make contact to usual extreme event statistics.

Lagrangian particle tracking. The particle tracking used in Fig. 4 works in the following way: we distribute a set of tracers over the lowest horizontal level ($z{=}50$ m) on the morning of the second day (1d6h). The set forms a squared lattice with one tracer placed every 4 km. The particles are then transported over a 24h-period using the horizontal velocity solution and a trapezoidal method with a 15-minute timestep. We choose to analyze the second simulation day because: (i) The horizontal morning moisture distribution is increasingly clustered from day to day. Thus earlier days a preferable for disentangling the dynamical effects of cold pools from the thermodynamic preconditioning. (ii) On the first day the rainfall is extremely sparse due to the spin-up from the initial condition. Still, repeating the analysis on later days gives comparable results. In the DIU-experiments we can seed tracers in the early morning when there is close to zero convective activity following the nocturnal cooling. This allows us to accurately capture the diurnal motion from onset of convection till the end of the last cold pools. In the RCE-experiments there are no such silent periods, so we have to pick arbitrary beginning and end times for the tracers. An animation of this process is presented in a supplemental video file.
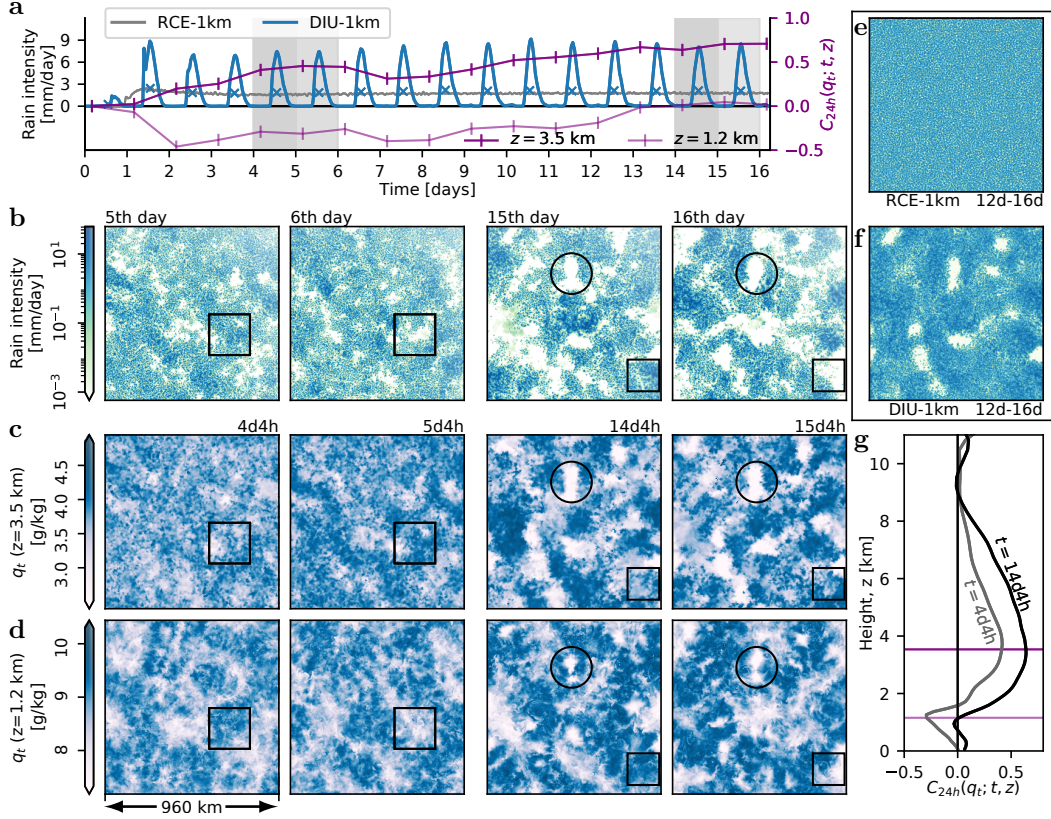
3 Results

How does the diurnal cycle affect the organization of convective clouds? To investigate this, we begin by examining two cloud resolving simulations, both with 1 km horizontal resolution: DIU-1km and RCE-1km. In DIU-1km, the surface temperature oscillates sinusoidally with a 24h-period and a 5K-amplitude to mimic the diurnal cycle (*Details*: Sec. 2). RCE-1km is a control experiment where the surface temperature is kept constant at the mean value of 298 K.

3.1 Two layers of convective organization

After a short spin-up period ($\sim$48h), rain intensity remains nearly constant in RCE-1km (Fig. 1a, gray curve). In DIU-1km, the oscillating $T_s(t)$ is reflected in oscillations in do-

Figure 1. Spatio-temporal organization by diurnal surface temperature oscillations. All data correspond to the DIU-1km experiment, except panel e and the gray curve in panel a which represent the RCE-1km experiment for comparison. **a**, Time series of domain-mean rain intensity in DIU-1km (blue curve) and RCE-1km (gray curve). Blue ×-symbols indicate daily-average rain intensity in DIU-1km. Dark and faint purple curves show time series of 24-hour Pearson correlations, $C_{24h}(q_t; t, z)$ for total water mixing ratio, q_t, for $z = 3.5$ km and $z = 1.2$ km respectively, with t taken at 4h on any given day (*Details:* Methods). **b**, Daily surface rainfall intensity for DIU-1km, temporally-averaged over the 5th, 6th, 15th and 16th day. Corresponding averaging periods indicated by gray shades in (a). **c**, Early-morning (4h) horizontal field of $q_t(t, x, y, z)$ for $z = 3.5$ km for DIU-1km at times corresponding to the days in (b). **d**, Analogous to (c) but for $z = 1.2$ km. Black squares and circles in (b)–(d) highlight regions discussed in the main text. **e**, Four-day average rain intensity on days 13–16 in RCE-1km. The color scale is the same as for panel (b). Note the lack of spatial organization. **f**, Analogous to (e), but for DIU-1km. Note the rain-free patches. **g**, $C_{24h}(q_t; t, z)$ vertical profiles, with $t = 4d4h$ (gray) and $t = 14d4h$ (black), respectively. The horizontal dark and faint purple lines indicate the respective vertical levels used in (a), (c) and (d).

main mean rain intensity, with a pronounced afternoon peak and mostly rain-free noc-
turnal conditions (Fig. 1a, blue curve). Daily-mean rainfall is, however, very similar in
the two experiments. Whereas RCE-1km shows no sign of CSA (Fig 1e), the spatial pat-
tern emerging in DIU-1km is strikingly different: during the first few days, the rainfall
develops a patchy mesoscale pattern with rain clusters measuring on the order of one hun-
dred kilometers across (Fig. 1b, 5th and 6th day) in compliance with previous findings
(Haerter et al., 2020). However, ten days later (days 15 and 16), the dynamics follows
a more complex pattern: in addition to the now larger and more intense MCSs, the do-
main is also spotted with persistently rain-free patches (marked as circled area). This
persistent lack of rainfall becomes particularly clear when considering rainfall averaged
during multiple days (Fig 1f).

The spatio-temporal pattern found in DIU-1km (Fig. 1b,c,d) seems to be a com-
position of two motifs related to separate mechanisms: (i) a negative feedback inhibit-
ing convective activity in areas where rain was particularly abundant the day before (ex-
amples are marked by squares); (ii) a positive feedback that can preserve inactivity from
day to day (an example is marked by circles). To analyze these feedbacks further, we turn
to the horizontal moisture field $q_t(z, t)$ at each vertical model level z and describe its tem-
poral evolution from night to night using the 24h-lag correlation $C_{24h}(q_t; t, z)$ (*Details:*
Methods). We choose early morning (4 am) as a reference because the moisture field is
diffusively smoothed due to the absence of convective activity during the night. The ver-
tical profile of $C_{24h}(q_t; t, z)$ reveals an interesting dynamical structure of two pronounced
extrema (Fig. 1g): a global minimum near 1.2 km and a global maximum near 3.5 km,
indicative of alternating moisture patterns at the lower but persistent moisture patterns
at the upper level. In the course of the simulation, the correlations generally increase to-
wards more positive values, and by day 14 even the minimum at 1.2 km takes positive
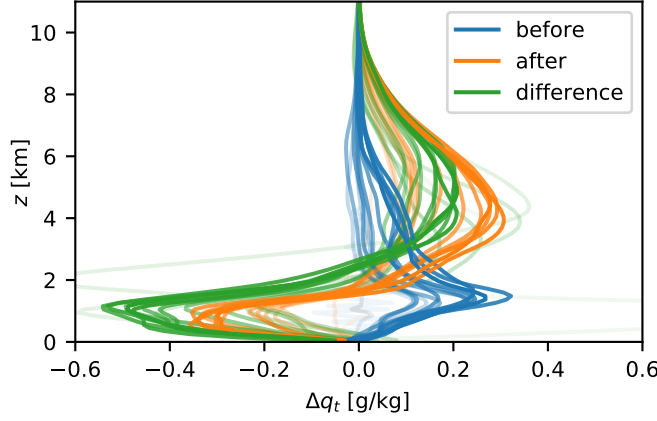values (Fig. 1a).

The moisture pattern at the lower level—corresponding approximately both to the
cloud base and the top of the boundary layer—closely mirrors that of the rainfall (*com-
pare* Fig. 1b and d). Examples are highlighted by black squares: at 4d4h, there is a strong
positive moisture anomaly at z=1.2 km. On the following (fifth) day, that region receives
intense rainfall, resulting in intense drying near the cloud base (at 5d5h). On the sixth
day, the area receives almost no rainfall.

The positive 24h-lag correlation in the free troposphere ($z = 3.5$ km) implies per-
sistence from day to day. Indeed, inspecting an example of one persistently dry patch
(circled in Fig. 1b,c,d), rainfall is absent in the same region during consecutive days. Rather
than replenishing the moisture within the persistently dry patches, rain clusters now ap-
pear to transport moisture elsewhere, undergoing day-to-day oscillatory dynamics that
specifically avoids the dry patches. Hence, despite the initial day-to-day alternation in
rainfall pattern, later days show sustained rain-free sub-regions—suggesting that the di-
urnal cycle opens a path to convective self-aggregation. Indeed, the persistent dry patches
closely resemble the early stages of CSA as observed in classical RCE studies. However,
as demonstrated by our control experiment, RCE-1km, no signs of CSA occur in our nu-
merical setup when surface temperature is constant—at least not within 16 simulation
days. Therefore, we conclude that the diurnal cycle can trigger CSA.

The dynamics described here is also observed in similar simulations with horizon-
tal resolution increased to 500 m. For this higher-resolution case, the analog to Fig. 1
is shown in Fig. S1. There, dry patches form significantly quicker and the negative peak
of $C_{24h}(q_t, z=1200m)$ vanishes at an earlier time within the simulation.

The 24h-lag correlation shows that different dynamics apply to moisture at differ-
ent altitudes, but it does not reveal much about the physical processes. To explain the
mechanism behind the correlations, it is useful to introduce the surface precipitation as
an intermediary variable. Most vertical transport occurs in deep convective clouds, which

Figure 2. **Moisture anomaly profiles before and after strong rain:** On each of the first 15 simulation days in DIU-1km, the total daily surface precipitation is calculated for each column, and the top 10% are marked as "rainy". Average moisture anomaly profiles for the "rainy" columns are then calculated at 4h the previous night (blue) and on the subsequent night (orange). The change in moisture from night to night, averaged over the "rainy" columns, is shown in green. Opacity increases linearly with time (faint curves represent early days).
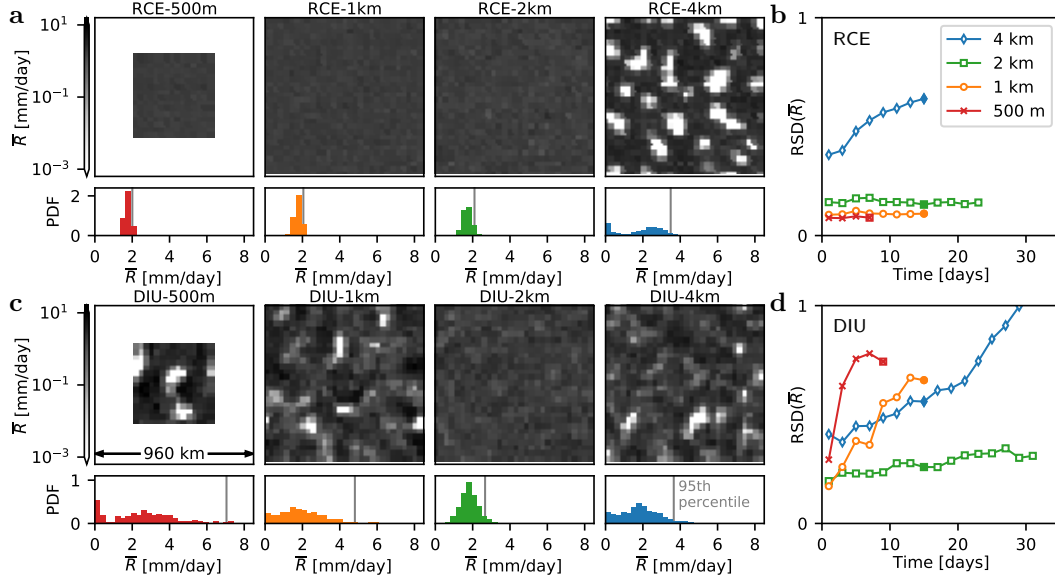
leave a strong signature in surface precipitation. We therefore investigate the spatial correlation between rainfall on a given day and the moisture profiles on the preceding and subsequent nights (Fig. 2). The blue curves show that strong rain is more likely to occur where the atmosphere was relatively moist in the early morning—especially around the cloud base ($z \approx 1.2$ km) but also at higher levels of the free troposphere. The orange curves show that where it rains, the boundary layer ($z \leq 1.5$ km) tends to dry out while the convective clouds tend to leave the free troposphere very moist. The green curves show that the average moisture tendency from night to night is indeed negative at low altitudes ($z \leq 2$ km) but positive in the free troposphere ($z \geq 2$ km) in the columns with top ten percent daily rainfall.

Using surface precipitation—a proxy for convective activity—as an intermediary variable, we can explain the moisture 24h-lag correlations as follows: high moisture at any altitude promotes convective activity. Convection lowers moisture in the boundary layer, giving rise to the negative correlations and the alternating DSA behavior. Convection also increases moisture in the free troposphere, which drives positive correlations and which can induce persistence.

3.2 Stronger clustering at higher resolutions

It is well known that fine horizontal resolution can hamper or even prevent CSA in the classical RCE framework. To study how resolution affects the emergence of persistent dry patches in combination with the active diurnal cycle, we conduct a series of simulations of horizontal resolution varying between .5, 1, 2, and 4 kilometers. For each case we contrast a setup where the surface temperature oscillates at an amplitude of 5 K (DIU) with a control experiment where the surface temperature is constant (RCE) (*Details:* Tab. 1).

CSA is characterized by large scale separation of the domain into dry areas without convective activity and moist areas with intense precipitation, but even patches of intense rainfall at scales of heavily-populated areas, such as large urban areas, can threaten society. To quantify such spatial rainfall variability we compute the relative standard deviation (RSD) of a coarse-grained rainfall field $\overline{R}$, where rainfall is block-averaged over

Figure 3. **Faster diurnal aggregation at higher resolution. a**, Classical CSA under RCE conditions, where the coarse-grained rainfall field $\overline{R}$ is shown at decreasing resolutions. Note that spatial patterns only emerge at coarse resolution (4 km). The bar plots show the histogram of $\overline{R}$ for the corresponding field in each panel. In the histograms the gray vertical lines indicate the respective 95th percentile. **b**, Time series of the relative standard deviation of $\overline{R}$ for each 48-hour period. **c** and **d**, Analogous to (a) and (b), but for DIU. Note that strong phase separation, akin to CSA, now increasingly occurs at finer resolution. Time points used in (a) and (c): RCE-500m: $t \in [6d, 8d]$, DIU-500m: $t \in [8d, 10d]$, all other cases: $t \in [14d0h, 16d0h]$, as indicated by the solid symbols in panels (b) and (d).

<div style="text-align: right">298</div> 32 km × 32 km horizontally and 48 hours temporally (*Details:* Methods). The 32 km
<div style="text-align: right">299</div> spatial scale is practically relevant as it corresponds to the size of large metropolitan ar-
<div style="text-align: right">300</div> eas. RSD hence quantifies the degree to which rainfall fluctuates at this specific scale.
<div style="text-align: right">301</div> The averaging procedure discounts both the small-scale fluctuations related to individ-
<div style="text-align: right">302</div> ual raincells and the day-to-day alternation related to the DSA dynamics.

<div style="text-align: right">303</div> RCE-4km shows a clear trend of increasing RSD($\overline{R}$), a typical feature of classical
<div style="text-align: right">304</div> CSA (Bretherton et al., 2005; Wing et al., 2017). However, for horizontal resolutions of
<div style="text-align: right">305</div> 2 km or finer, the RCE experiments show no sign of CSA (Fig. 3a,b) and RSD($\overline{R}$) re-
<div style="text-align: right">306</div> mains constant over time. This result agrees with the existing literature, which gener-
<div style="text-align: right">307</div> ally states that in RCE simulations, CSA is inhibited by fine horizontal model resolu-
<div style="text-align: right">308</div> tions (C. Muller & Bony, 2015; Wing et al., 2017).

<div style="text-align: right">309</div> In DIU, however, persistent rain-free patches are visible at 1 km resolution, result-
<div style="text-align: right">310</div> ing in RSD($\overline{R}$) rapidly increasing over time. The increase is even more pronounced in
<div style="text-align: right">311</div> DIU-500m, despite the smaller domain size which is also often considered detrimental
<div style="text-align: right">312</div> to CSA (C. J. Muller & Held, 2012; Jeevanjee & Romps, 2013; Yanase et al., 2020) (Fig. 3c,d).
<div style="text-align: right">313</div> In DIU-2km, RSD($\overline{R}$) shows a weaker increase and persistent rain-free patches are all
<div style="text-align: right">314</div> but absent (Fig. 3c,d). These observations lead us to conclude that the diurnal mech-
<div style="text-align: right">315</div> anism responsible for producing persistent dry patches is stronger with increasing hor-
<div style="text-align: right">316</div> izontal resolutions. At our coarsest resolution, DIU-4km also aggregates at a rate sim-
<div style="text-align: right">317</div> ilar to that of RCE-4km. However, based on the boundary-layer dynamics (Sec. 3.3), we
<div style="text-align: right">318</div> ascribe this to known CSA feedbacks, acting despite the diurnal cycle. Here we used the
<div style="text-align: right">319</div> RSD of block-averaged rainfall to quantify the degree of aggregation. Using $C_{24h}(q_t; z=3500m, t)$

as an alternative measure of persistent aggregation (Fig. S5), shows that increased day-to-day persistence is commensurate with increases in RSD. The findings on RSD mean that the likelihood of experiencing extreme convective rainfall at the scale of large urban settlements increases strongly, when the diurnal cycle is pronounced and when model resolution is high ($\leq 1km$ horizontally).
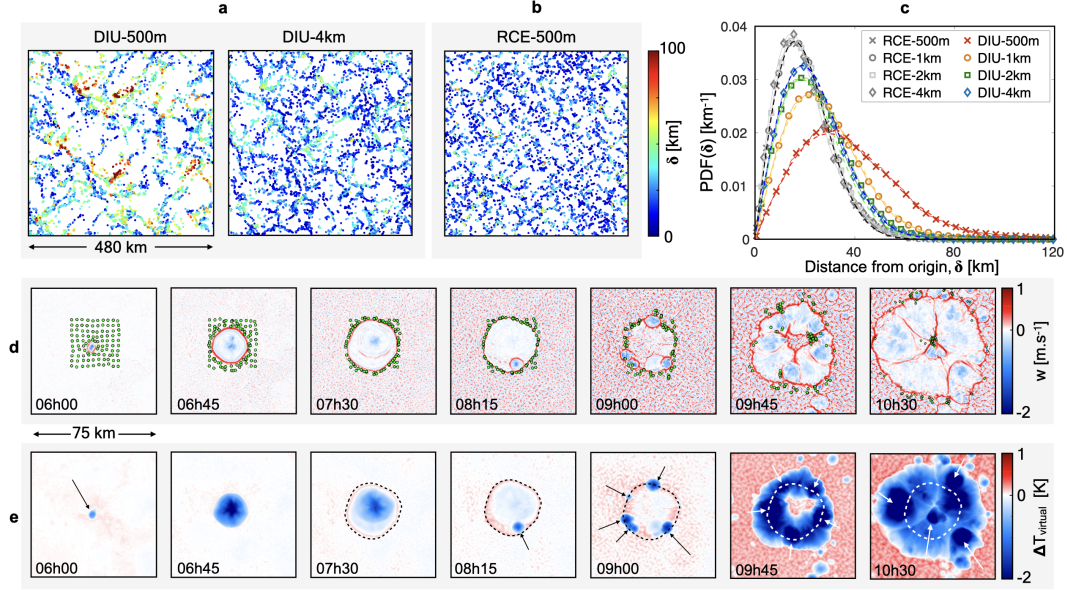
The current study mainly focuses on the emergence of persistent dry patches, but it is worth noticing that the diurnal cycle has a significant impact in the opposite, high, end of the precipitation distribution as well. Extreme precipitation is strongly enhanced for high resolutions in DIU (*see* vertical gray lines in Fig. 3c, lower panels, indicating the 95th percentiles). In RCE, extremes remain comparably small at such resolutions. The 99th percentile of daily rainfall—a typical index of extreme precipitation (Lenderink & Van Meijgaard, 2008)—increases fourfold in DIU compared to RCE at 500m and 1km horizontal resolutions, also measured at horizontal box-size of 32 km×32 km (Fig. S4). Hence, precipitation extremes can be strongly impacted by diurnal surface temperature oscillations even though the daily average temperature is not changed.

3.3 Convective cascades and combined CPs

Why does convective activity aggregate at high resolution for DIU but not for RCE? This section describes the cascading dynamics leading to large MCS-like rain events, combined CPs, and the day-to-day alternating spatial clustering described as "diurnal self-aggregation" (DSA) (Haerter et al., 2020). Section 3.4 will follow up with a case study showing how the large scale fluctuations induced by the diurnal cycle can give rise to persistently dry patches, a pattern closely resembling the early stage of standard CSA.

We examine the cascade of events leading to different organizational patterns in DIU versus RCE by mapping the low-level horizontal flow using Lagrangian particle tracking. Tracers are spaced regularly at time 1d6h, before the onset of precipitation, and passively advected with the horizontal flow during 24 hours (*Details*: Methods). In DIU-500m the final particle positions are visually clustered into stringy structures (Fig. 4a). Such patterns, which we attribute to the gust fronts of combined CPs produced by MCSs, are less pronounced in the coarser-resolution simulation DIU-4km. Also, particles in DIU-500m are generally displaced much further than in DIU-4km, with large cleared spaces opening up in DIU-500m (*compare* panels in Fig. 4a). To quantify these differences, we compute the distance between the initial and final position of each particle, termed δ. The set of distances for all particles yields a histogram of δ (Fig. 4c) for each simulation. These distributions are all well-fitted by Rayleigh functions: $P(\delta) = \pi(\delta/2\sigma) \exp[-\pi(\delta/2\sigma)^2]$. The Rayleigh function describes the radial part of a two-dimensional normal distribution and is consistent with the motion of a random walker. The diffusive length scale σ measures the typical distance traveled. Interestingly, σ systematically increases for DIU as the model resolution is made finer. In RCE, where particles cluster less than in DIU (Fig. 4a,b), the resolution has no noticeable effect on σ: it consistently remains smaller than for DIU (Fig. 4c, gray curves vs colored curves).
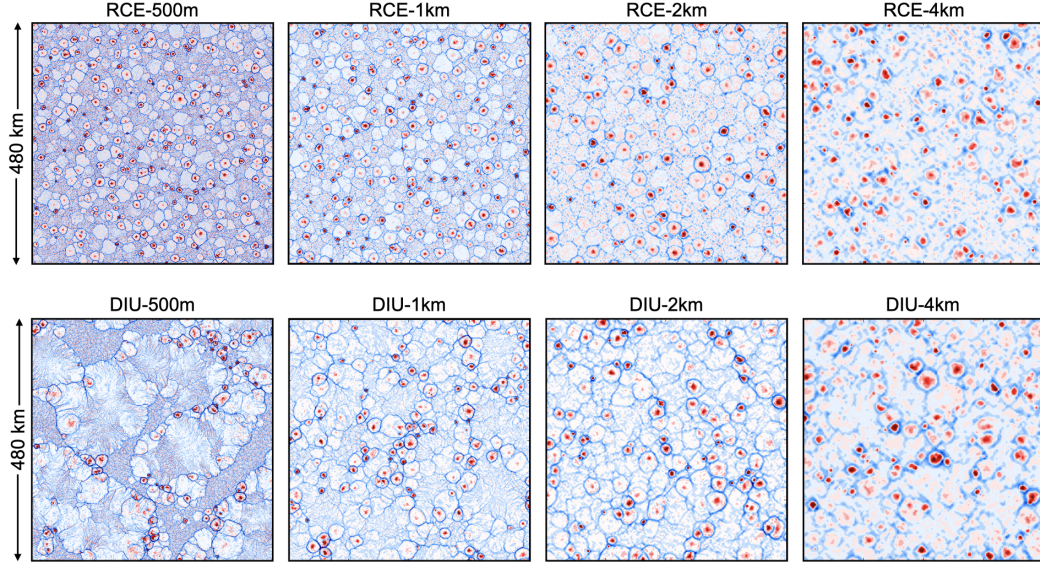
The continued increase of σ with finer resolution across all diurnal cases suggests that the aforementioned organizing processes become progressively activated as smaller length scales become explicitly resolved. Notably, the distribution of δ continues to broaden strongly, even between DIU-1km and DIU-500m, suggesting that the 500 m mesh is not yet sufficiently fine to fully activate all organizing processes. Hence, we do not think that numerical convergence has been yet attained. What are these small-scale processes which have such a dramatic impact on the low-level circulation? Why are these processes only relevant in DIU but not in RCE? RCE simulations are characterized by seemingly random eruptions of convective raincells and the associated spread of CPs with typical diameters of ∼10 km. These CPs are the main cause of horizontal winds, and they quickly

Figure 4. **Low-level circulation enhanced by resolution and diurnal cycle. a**, Final state of the Lagrangian particle tracking analysis in DIU. Tracers are seeded along a 4 km square lattice at 1d6h, and plotted at 2d6h and colored by the respective distance traveled, δ. **b**, Analogous to (a) but using RCE-500m. All RCE cases yielded a visually similar particle field and are not presented for conciseness. **c**, Probability distribution functions of δ. Dashed lines correspond to Rayleigh distribution best-fits. The best-fit scale parameters σ are $[37.1, 27.2, 24.3, 23.2]$ km for DIU for $dx = [0.5, 1.0, 2.0, 4.0]$ km, respectively, whereas $\sigma = 18.8 \pm 0.9$ km for RCE. **d**, Instantaneous vertical velocity fields at z=50 m during day 1 (exact times as labeled) showing the evolution of a *primo*-CP. 10×10 tracers, uniformly distributed on a square lattice with a spacing of 4 km, are initialized at 5h to visualize the surface flow. **e**, Analogous to (d) but for the virtual temperature anomaly field $\Delta T_{\text{virtual}}$ defined as the local difference to the (z=50 m)-horizontal average. Arrows highlight new CPs. The dashed line, shown in several panels, corresponds to the convergence ring of the *primo*-CP front once it has stopped its first expansion phase (*Details*: Methods).

transport tracers from their interior to the gust fronts. However, the disorganized occurrences of new CPs prevent the tracers from traveling long distances effectively.

Figure 5. **Contours of surface horizontal velocity divergence fields**. Instantaneous horizontal fields of $\frac{\partial u}{\partial y} + \frac{\partial v}{\partial x}$ for the first model level (z=50m) at 18h00 on the sixth day. The contours range from -0.004 to 0.004 s^{-1} (blue to red) and are presented from left to right in decreasing order of spatial resolution for both (top) RCE and (bottom) diurnal configurations.

By contrast, raincells in DIU occur in isolated diurnal bursts following the morning rise of surface temperature. As these bursts constitute the origin of the MCS we observe, we now discuss their evolution step by step (Figs. 4d,e). 6h00: as a result of morning heating, a primordial raincell forms, typically in a location of moderately enhanced moisture near the top of the boundary layer. Having "won" the daily *race to precipitation*, this specific location produces a cold pool—the first one of this day's precipitation cycle—which we term *primo-CP*. 6h45–7h30: with no other CPs in the vicinity "vying" for the same space, the primo-CP expands freely in a pristine environment ideally preconditioned by positively-buoyant Rayleigh-Bénard instabilities. Hence, the primo-CP's gust front propagates in a near-circular fashion until it has exhausted all of its negatively-buoyant potential energy. In this process it forms a *convergence ring*, marked by the green tracers and dashed lines in Fig 4d and e, respectively. 8h15-9h00: by further destabilizing the surrounding environment through positive vertical velocity, a primo-CP can set off a cascade of secondary raincell–CP pairs along its convergence ring. 10h30: the secondary CPs instigate a tertiary population and so forth.

Since such cascades of convective activity can last for several hours and span more than ∼100 km horizontally, we view them as emergent MCSs (Houze Jr, 2004). This process is driven by outward-running fronts merging into an enclosing macro-structure and we refer to it as a *combined CP* (Haerter et al., 2020). The large areas of the combined CPs result in a more persistent tracer transport (green points in Fig. 4d), explaining the increased mean δ's.

Similar MCS-like expansion processes occur throughout the model domain, on the same and on subsequent days. Eventually, later in the day, the interaction with other combined CPs and the decreasing surface heating halt further expansion. After the cascade is completed, a large region remains convectively suppressed by the reduced buoyancy of the cold and dry boundary layer (Fig. 4d,e, 10h30): as such, combined CPs are responsible for the negative day-to-day correlations of rainfall.

Importantly, two conditions have to be met to enable such cascades: (i) strong nocturnal cooling, ensuring quiescent conditions and a domain-wide reset of convection—and thus the existence of a primo-CP born from the first raincell which will inevitably occur as surface temperature rises in the morning. (ii) a mesh fine enough to resolve the convergence ring and the vertical mass fluxes at its edges—allowing the primo-CP to transition into a combined CP. Note that (i) cannot be satisfied by RCE, thus hampering combined CPs. Conversely, (ii) is likely not met by DIU-2km and DIU-4km where the coarse resolutions impede the cascading mechanism (*see* Fig. 5 for illustration).
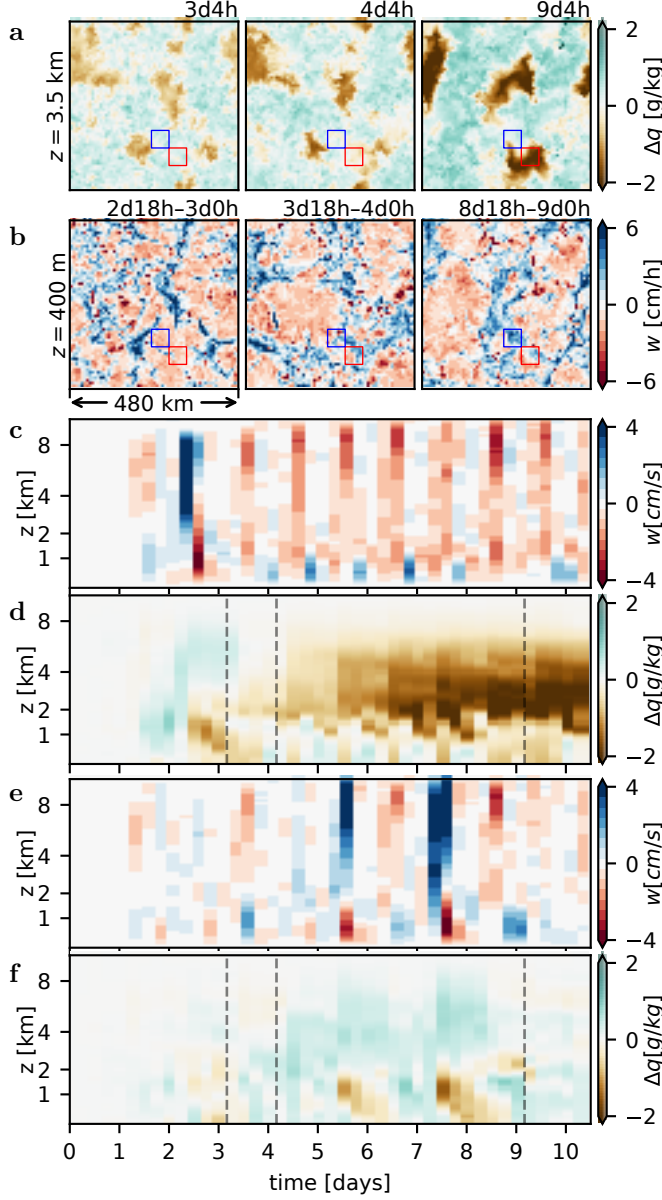
3.4 Genesis of a persistent dry patch

The cascade process proposed in Sec. 3.3 describes how—at high resolutions—the diurnal cycle gives rise to spatially clustered rainfall patterns alternating from day to day. But how are dry patches enabled that persist even longer, over many days? In order to answer this, we will more closely consider the onset of a particular persistent dry patch in DIU-500m (Fig. 6). The red squares in Fig. 6a,b mark a $50{\times}50$ km^2 sub-region where a dry patch emerges. By averaging variables horizontally within this region, we can visualize how the vertical structures and dynamics develop over time. The formation of the persistent dry patch is initiated by a strong MCS at time $t \approx 2$d12h (Fig. 6c). This process leaves the free troposphere relatively moist, but the boundary layer is dried out (Fig. 6d)—as is typical for columns with strong precipitation (Fig 2). On the following day, deep convection elsewhere forces pronounced subsidence within the region of interest. This subsidence leads to strong drying within the free troposphere, which experiences a change from a moist to a dry anomaly within a single day (Fig. 6d, $t \approx 3$d12h). At this stage, the resulting dry anomaly becomes self-sustaining. Convective activity is inhibited by dryness (Fig. 2) a feature attribute to the well-known moisture-radiation feedback invoked in studies on the maintenance of traditional CSA (Bretherton et al., 2005; C. J. Muller & Held, 2012; C. Muller & Bony, 2015; Yanase et al., 2020): the dry free troposphere (Fig. 6a,d) gives rise to increased long-wave cooling (*compare*: Fig. S3i–l), which in turn must be compensated by general subsidence heating. Subsidence further amplifies the drying and prevents deep convective activity.

In the boundary layer, a circulation is driven by the CP outflow from surrounding deep convective activity (Fig. 6b,4d18h-24h) and results in significant evening updrafts below $z \approx 1$ km between days four and eight (Fig. 6c). Such nocturnal low-level updrafts, however, do not initiate new convection because the atmosphere is already stabilized at this time of day.

Outside the dry patches, the dynamics switches from day to day between two modes (Fig. 6a,b blue boxes and e,f): on some days, most noticeably the sixth and the eighth day, mid-day convective activity results in heavy rainfall, increased free-tropospheric moisture, and significant boundary layer drying. On other days, such as the seventh and the nineth, the dynamics resembles that within the persistent dry patch, with net mid-day subsidence followed by low-level nocturnal updrafts (Fig. 6e). However, the mid-day subsidence is weaker than within the dry patch, and the free troposphere does not become drier than the domain average. Therefore, convection is no longer inhibited once the boundary layer has re-moistened. Rapid free-tropospheric drying appears to be a pivotal step in persistent dry patch formation. By contrast, in RCE-4km and DIU-4km, the onset of persistent dry patches seems to be a more gradual process starting from small scale fluctuations (Fig. S6).

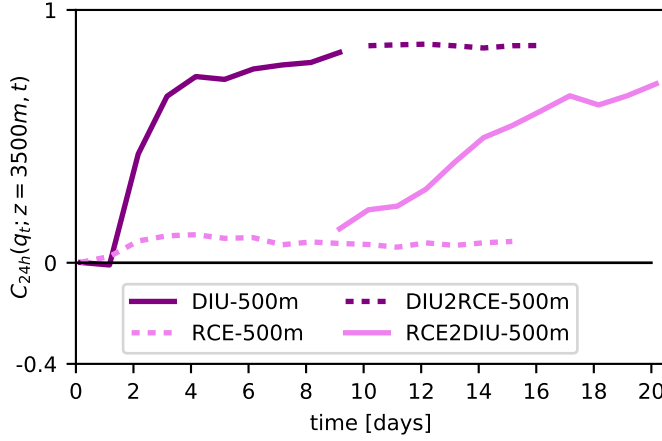### 3.5 Hysteresis of aggregation (the diurnal trigger)

The numerical experiments discussed so far made use of spatially homogeneous initial conditions. One may wonder if structured initial conditions influence the emergence of persistent dry patches in DIU-500m. To test for the impact of initial conditions we run

Figure 6. **Onset of a persistent dry patch.** All panels show data from DIU500m. **a**, Total water mixing ratio anomaly (Δq_t) at an altitude of $z \approx 3.5$ km (free troposphere). The three snapshots are taken at 3d4h, 4d4h, and 9d4h, as marked by dashed lines in panels d and f. A value of $\Delta q_t = 0$ corresponds to the horizontal domain average at the given time and altitude. The red square marks a 50×50 km^2 region where a persisten dry patch emerges. The blue square marks a region which remains convectively active. **b**, Vertical velocity (w) at an altitude of $z = 400$ m averaged in six hour intervals, 2d18h–3d0h, 3d18h–4d0h and 8d18h–9d0h, and horizontally smoothed by a Gaussian filter with a scale parameter $\sigma = 2$ km. **c**, Vertical velocity ($w(z,t)$) horizontally averaged over the same area as (c) (red squares). **d**, Total water mixing ratio anomaly ($\Delta q_t(z,t)$) horizontally averaged over the area marked in (a,b) by red squares. **e,f**, Analogous to (c,d), but averaged over the area marked by blue squares.

a new experiment, termed RCE2DIU-500m, where we use the state of the RCE-500m simulation at time 8d18h as an initial condition for a DIU simulation, where diurnal oscillations are then turned on. As both Fig. 1g and Fig. 6d suggest that persistent structures emerge from the free troposphere, we choose to quantify structure by the 24-hour autocorrelation of moisture at $z \approx 3.5\,km$ from night to night, $C_{24h}(q_t, z{=}3500\,\text{km}, t)$ (Fig. 7). Once the oscillations are turned on, $C_{24h}(q_t, z{=}3500m, t)$ starts increasing almost immediately, suggesting that the oscillations are indeed an effective mechanism to form dry patches in the free troposphere. The dynamics in RCE2DIU-500m are qualitatively very similar to the dynamics in DIU-500m. Quantitatively, the positive correlation in the free troposphere increase somewhat more slowly and the negative correlations near the top of the boundary layer remain longer. We attribute these two differences to greater stability of the final state of RCE-500m compared to our uniform initial conditions.

By contrast, when continuing the RCE-500m simulation without oscillations, persistence remains small and constant for several additional days. Further, its final state is characterized by regular small-scale moisture and rainfall patterns on the scale of individual cold pools, that is, approximately ten kilometers similar to that state shown in Fig. 5. This finite simulation can of course not prove that a much longer simulation would never aggregate, but at least it demonstrates that the persistent structures form much faster when the surface temperature is oscillating.

Figure 7. Hysteresis of CSA and the diurnal trigger. Timeseries of $C_{24h}(q_t; z, t)$ (*Details:* Methods) at $z = 3.5$ km. Solid and dashed curves represent oscillating and constant surface temperature simulations. Dark purple curves represent a numerical experiment, where initially oscillating surface temperatures (solid) are set constant after 9.75 days (dashed). Lighter purple curves represent a numerical experiment, where initially constant surface temperatures (dashed) are replaced by oscillating surface temperatures after 8.75 days.

Periodic surface temperature forcing can induce persistent dry patches, but can these dry patches prevail when the periodic forcing is removed? Such circumstances could come about in practice, when air masses are advected from land to sea, such as across the African west coast. To explore this, we now extend the DIU-500m simulation so that its state at time 9d18h serves as an initial condition for a simulation, termed DIU2RCE-500m, with the constant boundary conditions of RCE (Fig. S2). The Pearson autocorrelation is nearly maximal for $q_t(z{=}3.5\,\text{km})$, already at the end of the ten-day DIU-500m simulation. The switch to RCE gives rise to a persistently high autocorrelation. Additional analysis reveals that the classical CSA trademarks of increased long-wave cooling and the absence of rainfall over dry areas (Bretherton et al., 2005) are all present for DIU2RCE-500m (Fig. S3). Indeed, the state obtained after relaxation in DIU2RCE-500m shows

that outgoing long-wave radiation is increased over dry patches (Fig. S3i–k) and surface precipitation is all but absent (Fig. S3n–p). In summary, DIU2RCE-500m demonstrates that the atmosphere exhibits hysteresis: spatial patterns induced by a few days of diurnal oscillations can persist—and even intensify—without the oscillation. This result adds a new facet to a body of previous literature which also described hysteresis effects in relation to CSA (Khairoutdinov & Emanuel, 2010; C. J. Muller & Held, 2012; C. Muller & Bony, 2015; Holloway & Woolnough, 2016)

4 Summary and Discussion

This study set out to investigate the day-to-day alternating dynamics of MCS-like precipitation clusters referred to as diurnal self-aggregation (DSA) (Haerter et al., 2020). We found that the memory governing the negative precipitation autocorrelations can be traced back to the top of the atmospheric boundary layer, at $z \approx 1200$ m. However, the investigation also revealed a strong positive autocorrelation of moisture in the free troposphere, which we associated with persistent dry patches closely resembling the onset of classical convective self-aggregation (CSA). Such dry patches did not emerge in our control experiment with constant surface temperature and insolation. We, therefore, conclude that a temporally oscillating surface temperature can give rise to persistent spatial symmetry breaking by triggering CSA.

The diurnal path towards CSA. To further explore the newfound "diurnal path" to convective self-aggregation, we performed a set of simulations with varying horizontal resolutions (500 m, 1 km, 2 km, and 4 km), with and without surface temperature oscillations. Contrary to the usual constant surface temperature RCE framework where fine resolutions inhibit aggregation (C. J. Muller & Held, 2012; Jeevanjee & Romps, 2013; C. Muller & Bony, 2015), our simulations showed that fine resolution favors CSA when the diurnal cycle is active. Persistent dry patches emerged faster at 500 m compared to 1 km resolution, and at 2 km resolution we did not observe persistent dry patches at all. At our coarsest model resolution (4 km), we found clear signs of CSA both in the main experiment (DIU) and in the control (RCE). However, the onset of CSA in DIU-4km more closely resembles the dynamics in the RCE-4km than the dynamics in the high-resolution simulations. Previously, conceptual work attributed the onset of CSA to a linear instability in the free troposphere (Emanuel et al., 2014). By contrast, the onset of persistent dry patches in our high-resolution simulations is a highly non-linear process initiated by strongly correlated CP dynamics in the boundary layer: large combined CPs suppress convective activity for long enough to push the troposphere beyond the tipping point at which dry patches become self-perpetuating.

Strong hysteresis. The clustering dynamics revealed in the high-resolution simulation is subject to strong hysteresis. In a separate experiment, DIU2RCE, we demonstrated that dry patches induced over a few days with a strong diurnal cycle can persist, and even intensify, once the surface boundary condition reverts to a constant surface temperature. This finding makes us speculate: when organized convective cloud clusters, produced under a high-amplitude surface temperature forcing, are eventually advected over regions with little surface temperature variation, the clustered pattern may persist and even intensify further. Such a situation could be found at the interface between tropical continents and oceans, for example at the west coast of Africa. One could imagine that spatial inhomogeneities are: induced by the strong continental diurnal cycle, advected out over the Atlantic ocean by the easterly winds, and intensified despite the relatively weak sea surface temperature oscillations. However, more work is needed to clarify how large-scale advection affects the convective organization in combination with the diurnal cycle.

In summary, our numerical experiments show that diurnal temperature oscillations can enable CSA under conditions that would not allow it given constant surface tem-

peratures. This newfound diurnal path to convective self-aggregation is even stronger in the realistic limit of fine model resolution and subject to strong hysteresis.

Future questions. There are still open questions as to how the diurnal cycle affects convective organization.

(I) In the current study, we used a prescribed sinusoidal surface temperature oscillation with a diurnal range of 10 K around a mean of $\overline{T}_s = 298$ K and a Bowen ratio of $B \approx$ 0.30 (*Details:* Sec. 2). These conditions were intended to mimic forested continental conditions in the deep tropics where the Coriolis force is weak enough to be neglected. Indeed, diurnal temperature ranges average approximately ten kelvin for tropical and subtropical evergreen forests. In non-vegetated desert areas, however, daily fluctuations can be as large as 30 kelvins (Sharifnezhadazizi et al., 2019). Future work should therefore explore how larger diurnal surface temperature amplitudes affect convective self-aggregation, the formation of persistent dry patches and the spatio-temporal extent of the emergent mesoscale convective systems. Such analysis may give additional insight on the formation and maintenance of mesoscale convective systems in more arid regions with strong diurnal surface temperature ranges, such as the Sahel (Parker & Diop-Kane, 2017).

(II) Two-way interaction between a land surface and the local atmospheric conditions should be explored using a radiative diurnal cycle, in a fashion similar to that in Hohenegger and Stevens (2016) and Tompkins and Semie (2020), albeit using sub-kilometer horizontal resolutions and thinner slab layers, thus mimicking realistic continental diurnal cycles. In particular, the cooling effect of cold pools and cloud shading on the surface temperature should be incorporated within an interactive representation of the surface boundary condition. In RCE, recent studies have observed a negative feedback of surface responsiveness to CSA dynamics (Coppin & Bony, 2018; Shamekh et al., 2020). However, a highly-responsive surface would also result in a larger diurnal temperature range, potentially overcoming the negative feedback. Such a study could also offer new insight into the formation of oceanic storms where the amplitude of diurnal heating measured by satellite may have been under-estimated due to coarse resolution (Gentemann et al., 2008). It is therefore possible that diurnal sea surface temperature variations play a larger role than previously considered, especially in the extratropics where low-wind conditions are most prevalent (Gentemann et al., 2008). Even near the equator, such as for the western Pacific warm pool, diurnal sea surface temperature variations of three kelvins have been documented during low-wind conditions (Soloviev & Lukas, 1997). Given such evidence, temporal sea surface temperature variations might be sufficient to induce the persistent dry patches as we report them here.

Convective organization has important consequences also beyond local precipitation extremes. In fact, numerical modeling of large-scale thunderstorm clustering has been singled out as one of the fundamental questions relevant to the global climate (Bony et al., 2015). We hope that the current study will eventually help improve the connection between idealized experiments and empirical observations by raising awareness of the important effects resulting from temporal surface temperature fluctuations in general, and in particular the diurnal cycle.

Data Availability Statement

At `http://doi.org/10.5281/zenodo.4898182` a subset of the data produced within this study is available. These data contain summary timeseries as well as timeseries of vertical profiles of a number of variables for all 500 m simulations.

References

Bellenger, H., & Duvel, J.-P. (2009). An analysis of tropical ocean diurnal warm layers. *Journal of Climate*, *22*(13), 3629–3646.

Bellenger, H., Takayabu, Y., Ushiyama, T., & Yoneyama, K. (2010). Role of diurnal warm layers in the diurnal cycle of convection over the tropical indian ocean during mismo. *Monthly Weather Review*, *138*(6), 2426–2433.

Bony, S., Stevens, B., Frierson, D. M., Jakob, C., Kageyama, M., Pincus, R., . . . others (2015). Clouds, circulation and climate sensitivity. *Nature Geoscience*, *8*(4), 261–268.

Boye Nissen, S., & Haerter, J. O. (2019). Self-aggregation conceptualized by cold pool organization. *arXiv*, arXiv–1911.

Bretherton, C. S., Blossey, P. N., & Khairoutdinov, M. (2005). An energy-balance analysis of deep convective self-aggregation above uniform SST. *Journal of the Atmospheric Sciences*, *62*(12), 4273–4292.

Chen, S. S., & Houze, R. A. (1997). Diurnal variation and life-cycle of deep convective systems over the tropical pacific warm pool. *Quarterly Journal of the Royal Meteorological Society*, *123*(538), 357–388. doi: https://doi.org/10.1002/qj.49712353806

Coppin, D., & Bony, S. (2015). Physical mechanisms controlling the initiation of convective self-aggregation in a general circulation model. *Journal of Advances in Modeling Earth Systems*, *7*(4), 2060–2078.

Coppin, D., & Bony, S. (2018). On the interplay between convective aggregation, surface temperature gradients, and climate sensitivity. *Journal of Advances in Modeling Earth Systems*, *10*(12), 3123-3138. doi: https://doi.org/10.1029/2018MS001406

Craig, G., & Mack, J. (2013). A coarsening model for self-organization of tropical convection. *Journal of Geophysical Research: Atmospheres*, *118*(16), 8761–8769.

Cronin, T. W., Emanuel, K. A., & Molnar, P. (2015). Island precipitation enhancement and the diurnal cycle in radiative-convective equilibrium. *Quarterly Journal of the Royal Meteorological Society*, *141*(689), 1017–1034.

Dai, A. (2001). Global precipitation and thunderstorm frequencies. part ii: Diurnal variations. *Journal of Climate*, *14*(6), 1112–1128.

Emanuel, K. (2018). 100 years of progress in tropical cyclone research. *Meteorological Monographs*, *59*, 15–1.

Emanuel, K., Wing, A. A., & Vincent, E. M. (2014). Radiative-convective instability. *Journal of Advances in Modeling Earth Systems*, *6*(1), 75–90.

Fowler, H. J., Lenderink, G., Prein, A. F., Westra, S., Allan, R. P., Ban, N., . . . others (2021). Anthropogenic intensification of short-duration rainfall extremes. *Nature Reviews Earth & Environment*, *2*(2), 107–122.

Fritsch, J. M., & Carbone, R. (2004). Improving quantitative precipitation forecasts in the warm season: A uswrp research and development strategy. *Bulletin of the American Meteorological Society*, *85*(7), 955–966.

Gentemann, C. L., Minnett, P. J., Le Borgne, P., & Merchant, C. J. (2008). Multi-satellite measurements of large diurnal warming events. *Geophysical Research Letters*, *35*(22).

Haerter, J. O., Meyer, B., & Nissen, S. B. (2020). Diurnal self-aggregation. *npj Climate and Atmospheric Science*, *3*, 30.

Held, I. M., Hemler, R. S., & Ramaswamy, V. (1993). Radiative-convective equilibrium with explicit two-dimensional moist convection. *Journal of the Atmospheric Sciences*, *50*(23), 3909–3927.

Hirt, M., Craig, G. C., Schäfer, S. A., Savre, J., & Heinze, R. (2020). Cold-pool-driven convective initiation: using causal graph analysis to determine what convection-permitting models are missing. *Quarterly Journal of the Royal Meteorological Society*, *146*(730), 2205–2227.

Hohenegger, C., & Stevens, B.   (2016).   Coupled radiative convective equilibrium
simulations with explicit and parameterized convection.   *Journal of Advances
in Modeling Earth Systems*, *8*(3), 1468–1482.   doi: https://doi.org/10.1002/
2016MS000666

Holloway, C. E., & Woolnough, S. J.   (2016).   The sensitivity of convective ag-
gregation to diabatic processes in idealized radiative-convective equilibrium
simulations. *Journal of Advances in Modeling Earth Systems*, *8*(1), 166–195.

Houze Jr, R. A.   (2004).   Mesoscale convective systems.   *Reviews of Geophysics*,
42(4). doi: https://doi.org/10.1029/2004RG000150

Jeevanjee, N., & Romps, D. M.   (2013).   Convective self-aggregation, cold pools, and
domain size.   *Geophysical Research Letters*, *40*(5), 994–998.   doi: https://doi
.org/10.1002/grl.50204

Johnson, R. H., Rickenbach, T. M., Rutledge, S. A., Ciesielski, P. E., & Schubert,
W. H.   (1999).   Trimodal characteristics of tropical convection.   *Journal of
Climate*, *12*(8), 2397–2418.

Kawai, Y., & Wada, A.   (2007).   Diurnal sea surface temperature variation and its
impact on the atmosphere and ocean: A review.   *Journal of Oceanography*,
63(5), 721–744. doi: https://doi.org/10.1007/s10872-007-0063-0

Khairoutdinov, M. F., & Emanuel, K. A. (2010). Aggregated convection and the reg-
ulation of tropical climate. In *29th conference on hurricanes and tropical mete-
orology, amer. meteorol. soc., tucson, az.*

Lenderink, G., & Van Meijgaard, E.   (2008).   Increase in hourly precipitation ex-
tremes beyond expectations from temperature changes.   *Nature Geoscience*,
1(8), 511–514. doi: https://doi.org/10.1038/ngeo262

Liu, C., & Moncrieff, M. W.   (1998).   A numerical study of the diurnal cycle of
tropical oceanic convection.   *Journal of the Atmospheric Sciences*, *55*(13),
2329–2344.

Moseley, C., Hohenegger, C., Berg, P., & Haerter, J. O.   (2016).   Intensification of
convective extremes driven by cloud–cloud interaction.   *Nature Geoscience*,
9(10), 748. doi: https://doi.org/10.1038/ngeo2789

Moseley, C., Pscheidt, I., Cioni, G., & Heinze, R.   (2020).   Impact of resolution on
large-eddy simulation of midlatitude summertime convection.   *Atmospheric
Chemistry and Physics*, *20*(5), 2891–2910.

Muller, C., & Bony, S. (2015). What favors convective aggregation and why? *Geo-
physical Research Letters*, *42*(13), 5626–5634.   doi: https://doi.org/10.1002/
2015GL064260

Muller, C. J., & Held, I. M.   (2012).   Detailed investigation of the self-aggregation
of convection in cloud-resolving simulations.   *Journal of the Atmospheric Sci-
ences*, *69*(8), 2551–2565. doi: https://doi.org/10.1175/JAS-D-11-0257.1

Muller, C. J., & Romps, D. M.   (2018).   Acceleration of tropical cyclogenesis by
self-aggregation feedbacks.   *Proceedings of the National Academy of Sciences*,
115(12), 2930–2935.

Parker, D. J., & Diop-Kane, M.   (2017).   *Meteorology of tropical west africa: The
forecasters' handbook*. John Wiley & Sons.

Peatman, S. C., Matthews, A. J., & Stevens, D. P.   (2014).   Propagation of the
madden–julian oscillation through the maritime continent and scale interac-
tion with the diurnal cycle of precipitation.   *Quarterly Journal of the Royal
Meteorological Society*, *140*(680), 814–825.

Pincus, R., & Stevens, B.   (2009).   Monte Carlo spectral integration: A consistent
approximation for radiative transfer in large eddy simulations.   *Journal of Ad-
vances in Modeling Earth Systems*, *1*(2). doi: https://doi.org/10.3894/JAMES
.2009.1.1

Prein, A. F., Liu, C., Ikeda, K., Bullock, R., Rasmussen, R. M., Holland, G. J., &
Clark, M.   (2017).   Simulating North American mesoscale convective systems
with a convection-permitting climate model.   *Climate Dynamics*, 1–16.   doi:

https://doi.org/10.1007/s00382-017-3993-2

Ruppert Jr, J. H., & Hohenegger, C. (2018). Diurnal circulation adjustment and organized deep convection. *Journal of Climate*, *31*(12), 4899–4916. doi: https://doi.org/10.1175/JCLI-D-17-0693.1

Ruppert Jr, J. H., & O'Neill, M. E. (2019). Diurnal cloud and circulation changes in simulated tropical cyclones. *Geophysical Research Letters*, *46*(1), 502–511. doi: https://doi.org/10.1029/2018GL081302

Schumacher, R. S., & Rasmussen, K. L. (2020). The formation, character and changing nature of mesoscale convective systems. *Nature Reviews Earth & Environment*, *1*(6), 300–314.

Seifert, A., & Beheng, K. (2006). A two-moment cloud microphysics parameterization for mixed-phase clouds. Part 1: Model description. *Meteorology and Atmospheric Physics*, *92*(1-2), 45–66. doi: https://doi.org/10.1007/s00703-005-0113-3

Shamekh, S., Muller, C., Duvel, J.-P., & D'Andrea, F. (2020). Self-aggregation of convective clouds with interactive sea surface temperature. *Journal of Advances in Modeling Earth Systems*, *12*(11), e2020MS002164. Retrieved from https://agupubs.onlinelibrary.wiley.com/doi/abs/10.1029/2020MS002164 (e2020MS002164 10.1029/2020MS002164) doi: https://doi.org/10.1029/2020MS002164

Sharifnezhadazizi, Z., Norouzi, H., Prakash, S., Beale, C., & Khanbilvardi, R. (2019). A global analysis of land surface temperature diurnal cycle using modis observations. *Journal of Applied Meteorology and Climatology*, *58*(6), 1279–1291.

Smagorinsky, J. (1963). General circulation experiments with the primitive equations: I. the basic experiment. *Monthly Weather Review*, *91*(3), 99–164.

Soloviev, A., & Lukas, R. (1997). Observation of large diurnal warming events in the near-surface layer of the western equatorial pacific warm pool. *Deep Sea Research Part I: Oceanographic Research Papers*, *44*(6), 1055–1076.

Stevens, B., Moeng, C.-H., Ackerman, A. S., Bretherton, C. S., Chlond, A., de Roode, S., ... Zhu, P. (2005). Evaluation of large-eddy simulations via observations of nocturnal marine stratocumulus. *Monthly Weather Review*, *133*(6), 1443–1462. doi: https://doi.org/10.1175/MWR2930.1

Stull, R. B. (2012). *An introduction to boundary layer meteorology* (Vol. 13). Springer Science & Business Media.

Sukovich, E. M., Ralph, F. M., Barthold, F. E., Reynolds, D. W., & Novak, D. R. (2014). Extreme quantitative precipitation forecast performance at the weather prediction center from 2001 to 2011. *Weather and forecasting*, *29*(4), 894–911.

Suzuki, T. (2009). Diurnal cycle of deep convection in super clusters embedded in the Madden-Julian Oscillation. *Journal of Geophysical Research: Atmospheres*, *114*(D22). doi: https://doi.org/10.1029/2008JD011303

Tan, J., Jakob, C., Rossow, W. B., & Tselioudis, G. (2015). Increases in tropical rainfall driven by changes in frequency of organized deep convection. *Nature*, *519*(7544), 451–454. doi: https://doi.org/10.1038/nature14339

Tian, B., Waliser, D. E., & Fetzer, E. J. (2006). Modulation of the diurnal cycle of tropical deep convective clouds by the MJO. *Geophysical Research Letters*, *33*(20). doi: https://doi.org/10.1029/2006GL027752

Tompkins, A. M., & Craig, G. C. (1998). Radiative–convective equilibrium in a three-dimensional cloud-ensemble model. *Quarterly Journal of the Royal Meteorological Society*, *124*(550), 2073–2097. doi: https://doi.org/10.1002/qj.49712455013

Tompkins, A. M., & Semie, A. G. (2020). Impact of a mixed ocean layer and the diurnal cycle on convective aggregation. *Journal of Advances in Modeling Earth Systems*, e2020MS002186.

Weller, R., & Anderson, S. (1996). Surface meteorology and air-sea fluxes in the western equatorial pacific warm pool during the toga coupled ocean-

750   atmosphere response experiment. *Journal of Climate*, *9*(8), 1959–1990.

751   Westra, S., Fowler, H., Evans, J., Alexander, L., Berg, P., Johnson, F., . . . Roberts,
752   N.   (2014).   Future changes to the intensity and frequency of short-duration
753   extreme rainfall. *Reviews of Geophysics*, *52*(3), 522–555.

754   Wing, A. A., Emanuel, K., Holloway, C. E., & Muller, C.   (2017).   Convective self-
755   aggregation in numerical simulations: a review.   *Surveys in Geophysics*, *38*(6),
756   1173–1197.

757   Yanase, T., Nishizawa, S., Miura, H., Takemi, T., & Tomita, H.   (2020).   New criti-
758   cal length for the onset of self-aggregation of moist convection. *Geophysical Re-
759   search Letters*, *47*(16), e2020GL088763.

760   Zhang, C. (2005). Madden-Julian Oscillation. *Reviews of Geophysics*, *43*(2).